Supporting Information

Modulation of coordination environment enhances electrocatalytic efficiency of Mo single atoms toward water splitting

Chih-Chieh Cheng,[a] Yong-Xian Yeh,[a] Yu-Chieh Ting,[a] Shin-Hong Lin,[a] Kotaro Sasaki,[b] YongMan Choi,[c] Shih-Yuan Lu[a]**

Affiliations:

[a]Department of Chemical Engineering, National Tsing Hua University, Hsinchu 30013, Taiwan.

[b]Chemistry Department, Brookhaven National Laboratory, Upton, NY 11973, USA.

[c]College of Photonics, National Yang Ming Chiao Tung University, Tainan 71150, Taiwan.

Email: *ymchoi@nctu.edu.tw* ***(Y. Choi)****;* *sylu@mx.nthu.edu.tw* ***(S.-Y. Lu)***

Computational methods

All spin-polarized periodic density functional theory (DFT) calculations were performed using the Vienna Ab initio Simulation Package (VASP)[1-2] to systematically examine the HER activity of the three single-atom catalysts (SACs) of Mo-O_2C_2, Mo-$O_2N_1C_1$, and Mo-O_2N_2. We used revised Perdew-Burke-Ernzerh (RPBE) functional[3] within the generalized gradient approximation (GGA) for modeling the exchange-correlation energy and the projector augmented plane wave (PAW) method[4] for describing ionic cores. The tetrahedron method with Blöchl corrections of $\sigma = 0.05$ eV was employed, while 600 eV of the plane-wave cutoff energy was used. To prepare 2D-slab models for Mo-O_2C_2, Mo-$O_2N_1C_1$, and Mo-O_2N_2, a bulk graphite model (hexagonal, *P63/mmc*) was first prepared. To get accurate lattice constants of the bulk graphite (Figure S17),[5] Brillouin-zone integrations were performed on a grid of (12 × 12 × 8) **k**-point meshes with the Monkhorst–Pack method.[6] (3 × 3 × 1) **k**-point meshes were used for 2D-slab model calculations. Our computational method using the DFT-D3 method in the RPBE level (RPBE/DFT-D3) reproduced the experimental value of the graphite interlayer spacing[5] at 4.2 K (3.336 Å versus 3.3111 Å, respectively). In addition, we compared the reference value of hydrogen adsorption energy and its Gibbs free energy on p(2 × 2) four-layered Pt(111)[7] in the RPBE level. As shown in Figure S17, the hexagonally networked graphite layers are combined by van der Waals forces with an interval of 3.3111 Å and a CC-bond length of 1.4273 Å. The calculated lattice parameters a = 2.4722 Å and c = 6.6222 Å are in line with the experimental values.[5, 8] As its (0001) facet is the basal plane and principally exposed,[9] we first applied the three-layer (0001) surface for generating Mo-containing SAC models. Figure S17 and Figure S18, respectively, show the structures of bulk graphite and a periodically extended 6 × 6 surface model (216 C atoms) with 15 Å of a vacuum space to separate the slabs. The bottom two layers were fixed to the bulk properties. Then, we generated four-coordinated Mo centers by following the experimental results. For the three-layer model, only the top-most layer and the adsorbate (*i.e.*, hydrogen atoms) were allowed to fully relax, whereas its bottom two layers were fixed at the bulk properties. A one-layer graphene model was examined to save computational time as shown in Figure S18. We confirmed that the difference of hydrogen adsorption energies between one- and three-layer models (~0.3 eV) may be negligible. Then, the one-layer model was used to propose plausible surface configurations supporting the experimental findings via extensive calculations. To verify the computational approach, as summarized in Table S3, a (2 × 2) surface of Pt(111) (16 Pt atoms) was applied. Only the most stable three-fold fcc active site was used for obtaining hydrogen adsorption energies. Without applying the dispersion correction, it agrees with that in the literature.[7] To accurately evaluate the HER activity of Mo-O_2C_2, Mo-$O_2N_1C_1$, and Mo-O_2N_2, the Gibbs free

energy change of hydrogen adsorption (ΔG_H) is used as a crucial descriptor and defined as the following expression.[7]

$$\Delta G_H = \Delta E_H - T\Delta S_H + \Delta E_{ZPE} \quad (1)$$

where ΔE_H is the adsorption energy of a hydrogen atom adsorbed at the Mo metal center of the SAC.

$$\Delta E_H = E(H\text{-}SAC) - E(SAC) - 1/2E(H_2) \quad (2)$$

where E(H-SAC), E(SAC), and E(H_2) are the calculated energies of the SAC with an adsorbed hydrogen species, the clean SAC surface, and gas-phase H_2, respectively. ΔS_H and ΔE_{ZPE} are the entropy difference and zero-point energy (ZPE) of adsorbed hydrogen and gas-phase hydrogen, respectively. T is the temperature at 298.15 K. As the vibrational entropy term of an adsorbed hydrogen atom is negligible (Table S3), the entropy change is approximated by using $\Delta S_H \cong -\frac{1}{2}S^0_{H_2}$ at the standard conditions. ZPEs are calculated by $E_{ZPE} = \sum_{i=1}^{n}\frac{1}{2}h\nu_i$, where ν_i is the vibrational frequency. The Dmol^3 module[10-11] implemented in the Materials Studio package[12] was used to obtain the correction energy of the Gibbs free energy ($-T\Delta S_H + \Delta E_{ZPE}$) using the optimized geometries from VASP calculations. The double numerical polarization (DNP) 4.4 basis, the all-electron method, and the RPBE exchange-correlation functional were applied for the single-point energy calculations. As summarized in Table S3, the correction energy is close to the value reported in the literature and is a constant. The minor discrepancy results from different computational methods. Therefore, to be consistent with the literature,[7] we used the literature value of 0.24 eV, and the overall correction is taken as $\Delta G_H = \Delta E_H + 0.24\ eV$. The charge density difference was calculated according to the following expression

$$\Delta\rho = \rho_{H-SAC} - (\rho_{SAC} + \rho_H)$$

where $\rho_{H\text{-}SAC}$, ρ_{SAC}, and ρ_H are the charge density of Mo SAC with adsorbed H, SAC, and H, respectively. The charge density differences were rendered using VESTA.[13]

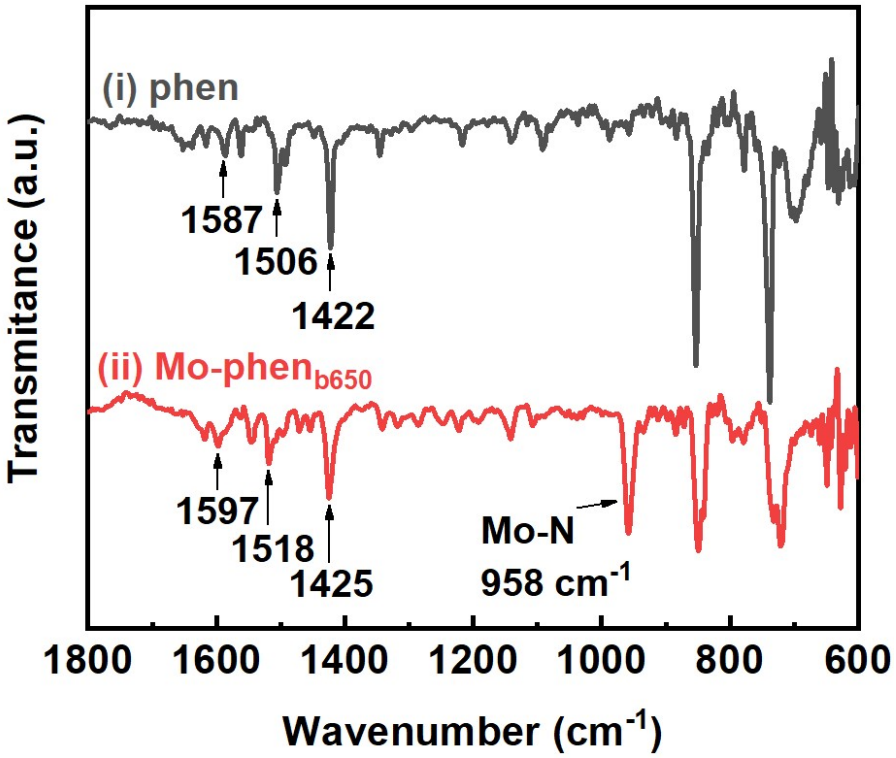

Figure S1. ATR-FTIR spectra of phen and Mo-phen$_{b650}$.

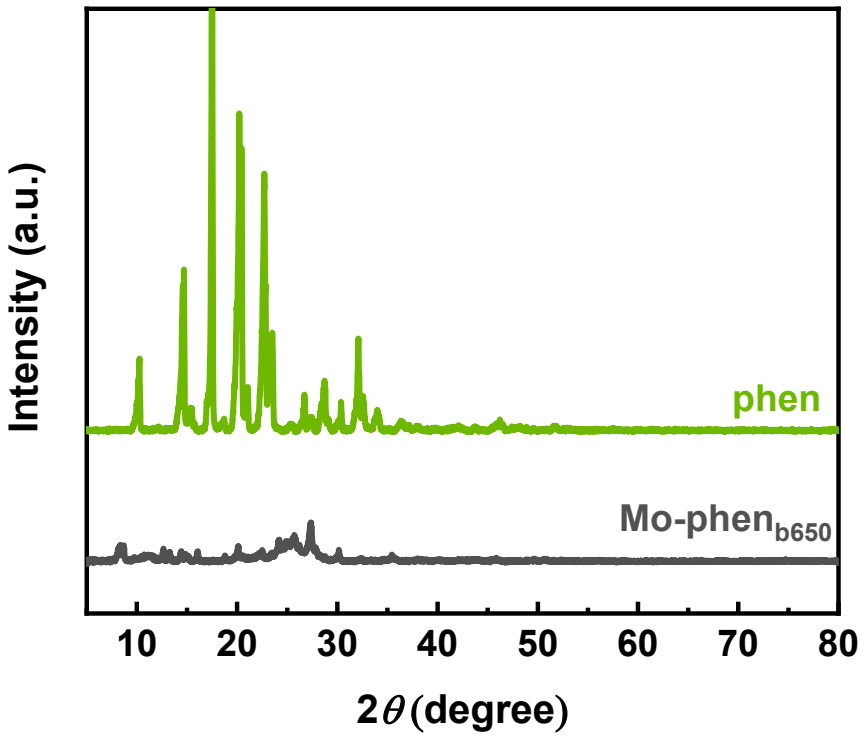

Figure S2. Powder XRD patterns of phen and Mo-phen$_{b650}$.

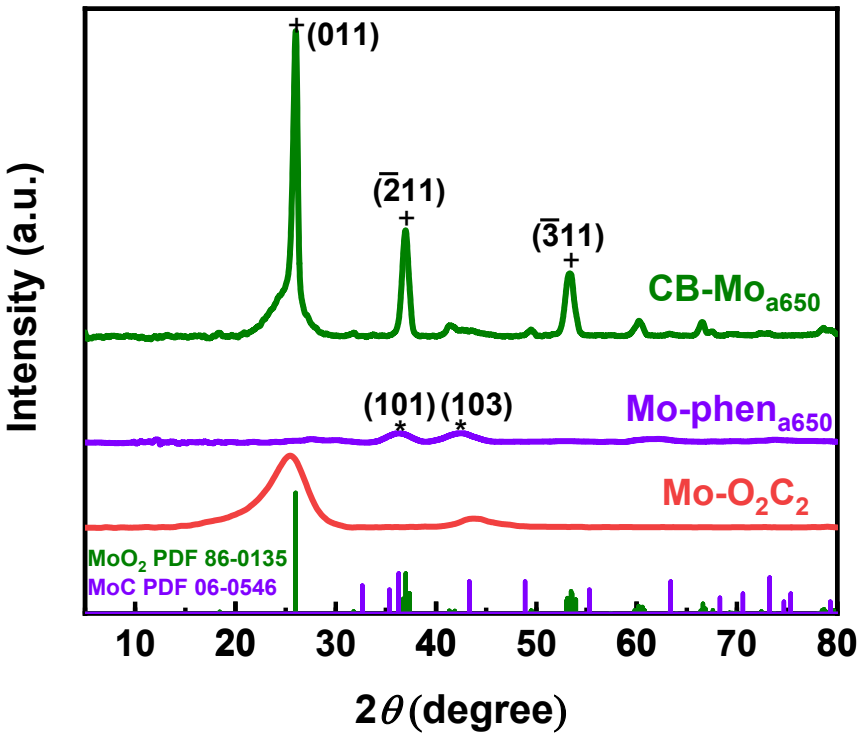

Figure S3. Powder XRD patterns of CB-Mo_{a650}, Mo-$phen_{a650}$, and Mo-O_2C_2.

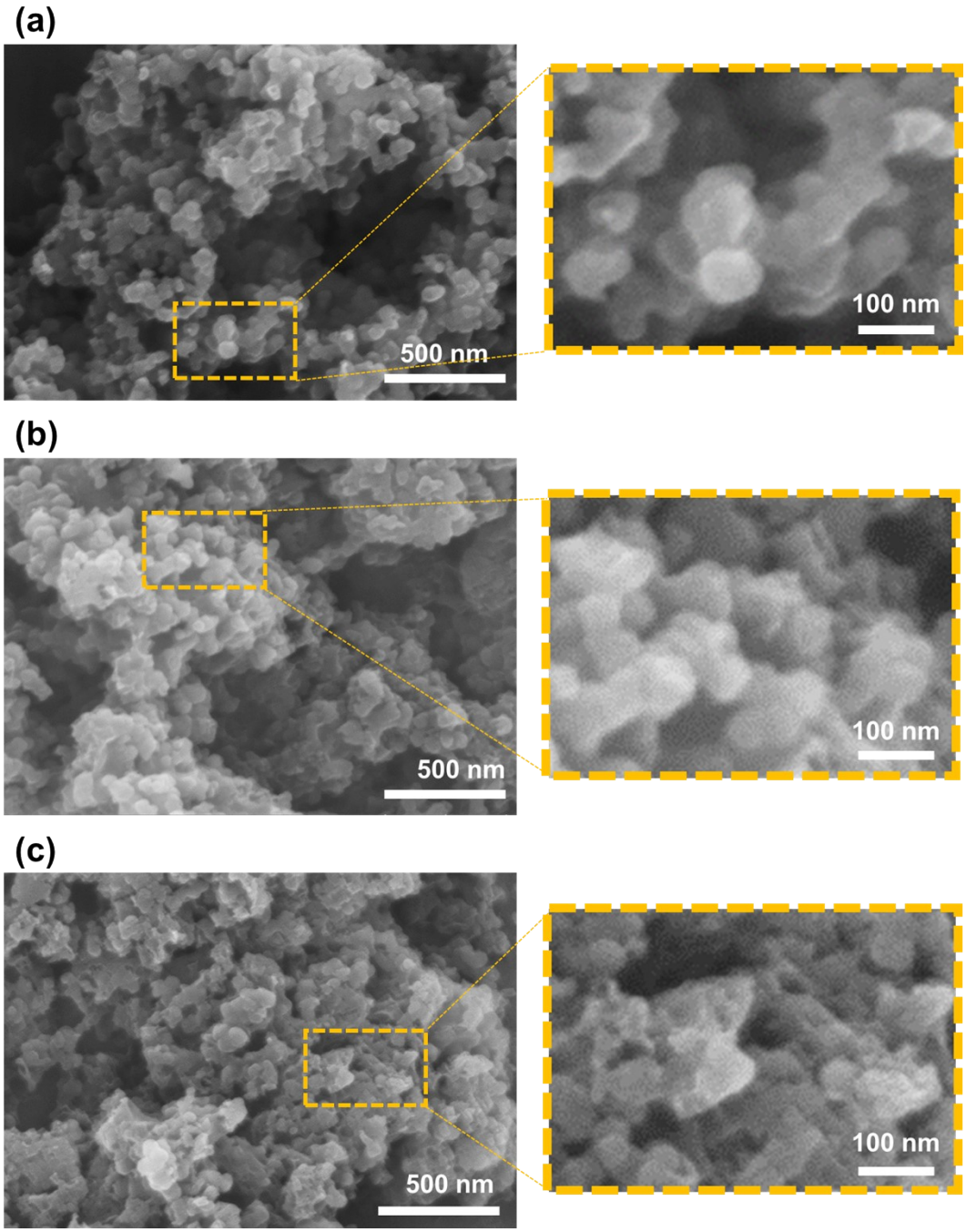

Figure S4. SEM images of (a) Mo-O_2C_2, (b) Mo-$O_2N_1C_1$, and (c) Mo-O_2N_2.

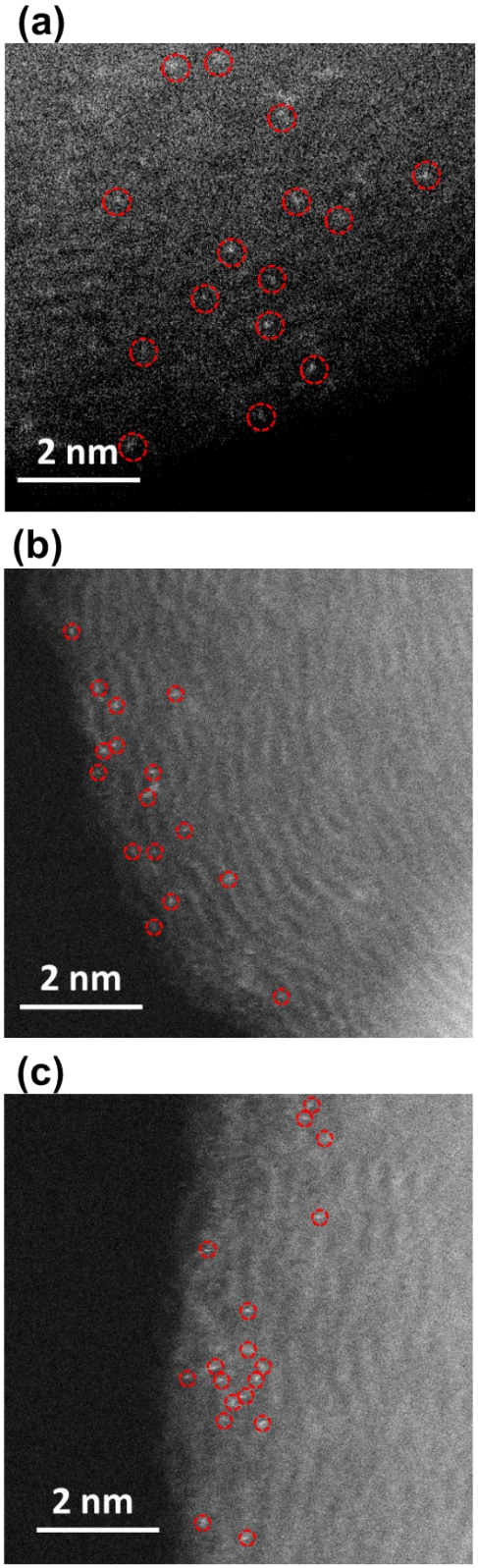

Figure S5. High magnification HAADF-STEM images of (a) Mo-O_2C_2, (b) Mo-$O_2N_1C_1$, and (c) Mo-O_2N_2.

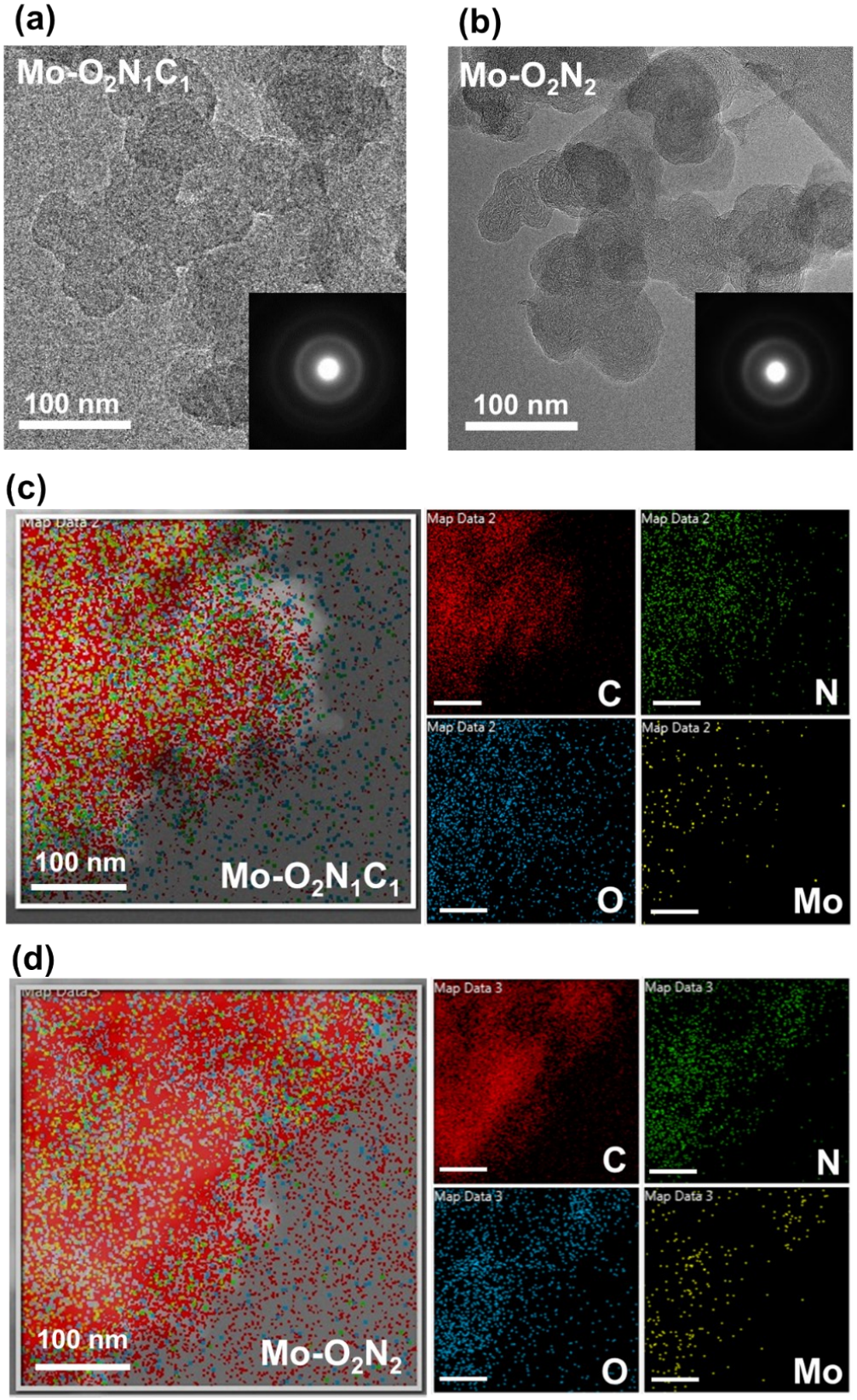

Figure S6. HR-TEM images and corresponding SAED patterns (inset) of (a) Mo-$O_2N_1C_1$ and (b) Mo-O_2N_2. EDS elemental mapping of (c) Mo-$O_2N_1C_1$ and (d) Mo-O_2N_2 (scale bar: 100 nm).

Table S1. Optimal fitting results for EXAFS data of Mo-O_2C_2, Mo-$O_2N_1C_1$, and Mo-O_2N_2.

catalyst	path	*C.N.*[a]	*R*(Å)[b]	$\triangle E_0$ (eV)[c]	σ^2(Å^2) [d]	*R* factor[e]
Mo-O_2C_2	Mo-O	2.26±0.09	1.72	-7.24	0.0020	0.004
	Mo-C	2.08±0.29	1.98		0.0071	
Mo-$O_2N_1C_1$	Mo-O	2.08±0.08	1.70	-6.70	0.0020	0.002
	Mo-C	0.82±0.13	2.02		0.0090	
	Mo-N	0.79±0.20	2.18		0.0030	
Mo-O_2N_2	Mo-O	2.06±0.07	1.74	-8.50	0.0021	0.002
	Mo-N	1.79±0.24	2.14		0.0080	

[a]*C.N.*, coordination number; [b]*R*, distance between absorber and backscatter atoms; [c]$\triangle E_0$, inner potential correction; [d]σ^2, Debye-Waller factor, thermal and structural disorders; [e]*R* factor, an indicator of fitting accuracy. S_0^2 was set to 0.95. Fitting ranges were all set to $1.0 < R < 2.0$ Å.

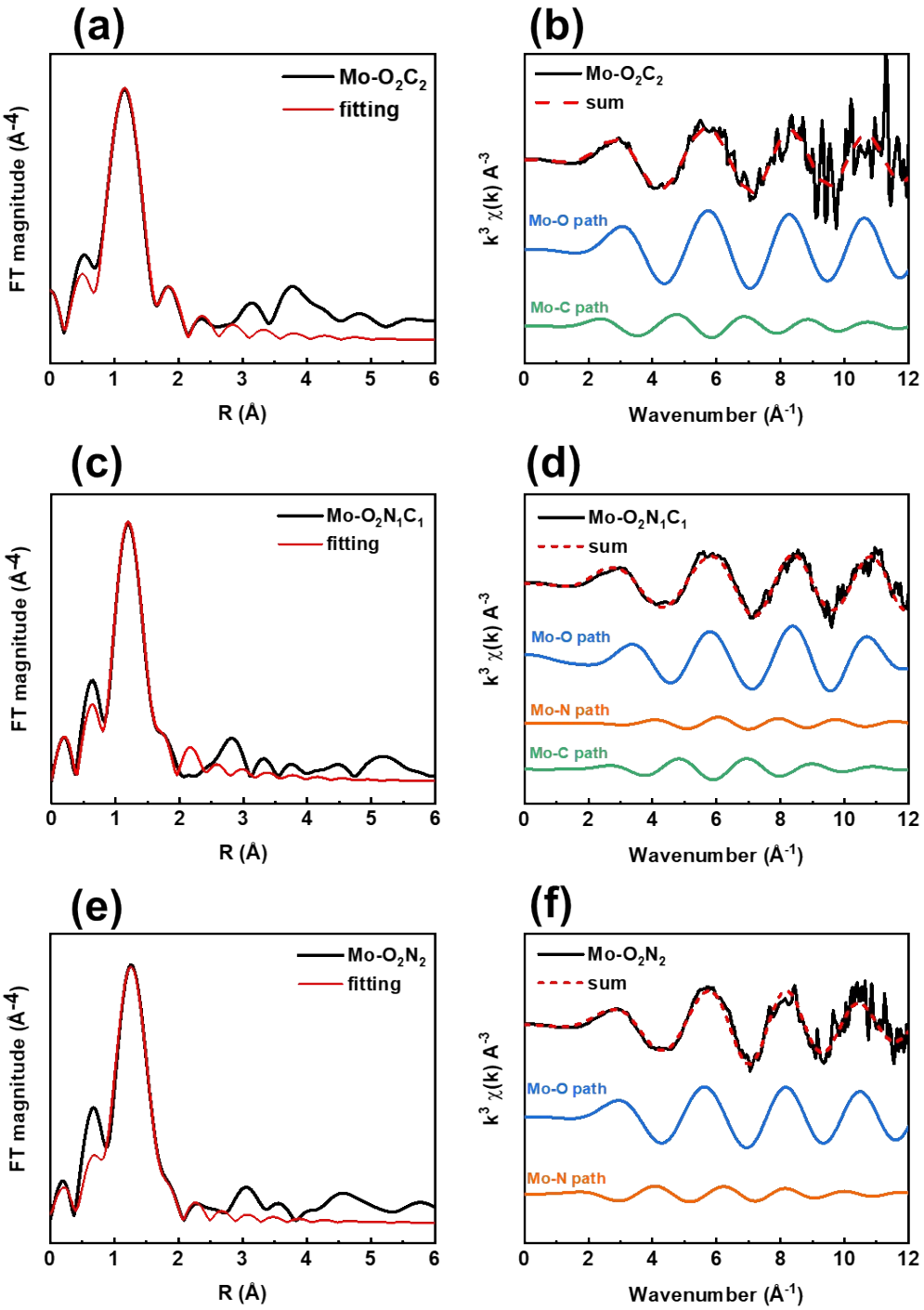

Figure S7. First-shell fitting of k^3-weighted EXAFS in R space and inversed FT-EXAFS fitting paths in k space. (a) and (b) Mo-O_2C_2, (c) and (d) Mo-$O_2N_1C_1$, (e) and (f) Mo-O_2N_2. Fitting ranges were all set to $1.0 < R < 2.0$ Å.

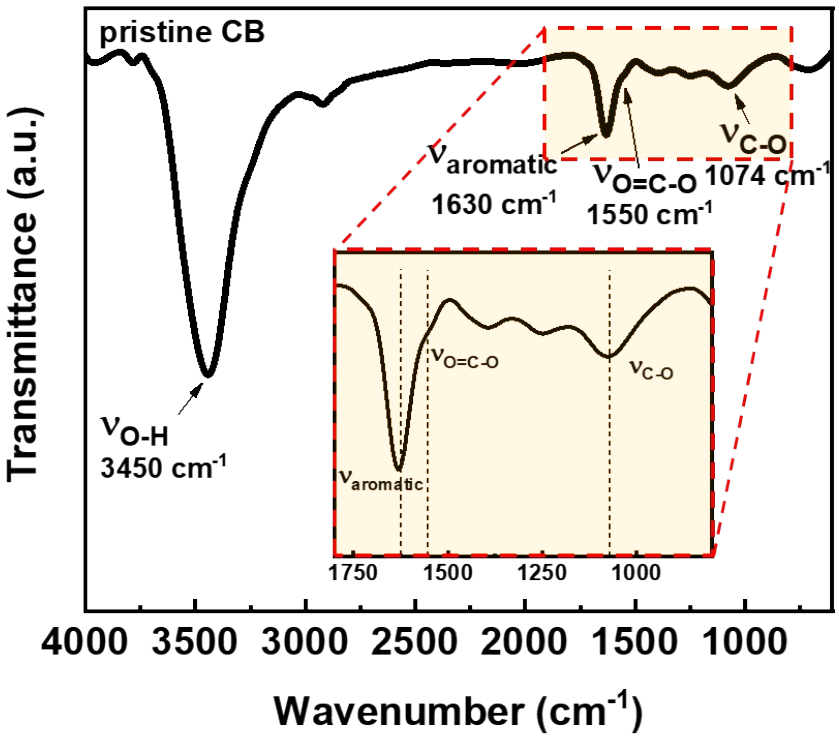

Figure S8. FTIR spectrum of CB.

Table S2. Summary of precursors and N/C molar ratios for fabrication of Mo SACs.

sample	precursor	N/C molar ratio in precursor
Mo-O_2C_2	CB (150 mg), phen (216 mg)	0.08 (100% from phen, 0% form DCD)
Mo-$O_2N_1C_1$	CB (150 mg), phen (216 mg), DCD (100 mg)	0.25 (32% from phen, 68% from DCD)
Mo-O_2N_2	CB (150 mg), phen (216 mg), DCD (200 mg)	0.39 (18% from phen, 82% from DCD)

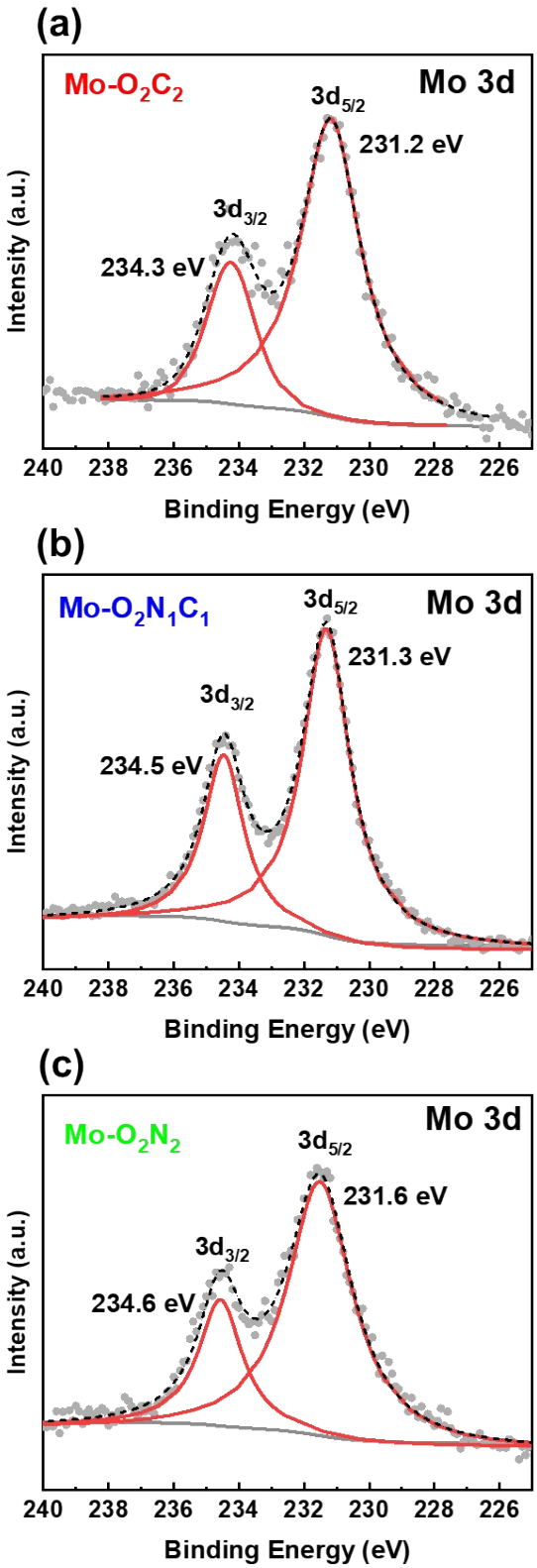

Figure S9. HR-XPS spectra of (a) Mo-O_2C_2, (b) Mo-$O_2N_1C_1$, and (c) Mo-O_2N_2 with fitted Mo $3d_{5/2}$ and Mo $3d_{3/2}$ curves plotted in red, and accumulation of fitted peaks plotted in black dashes.

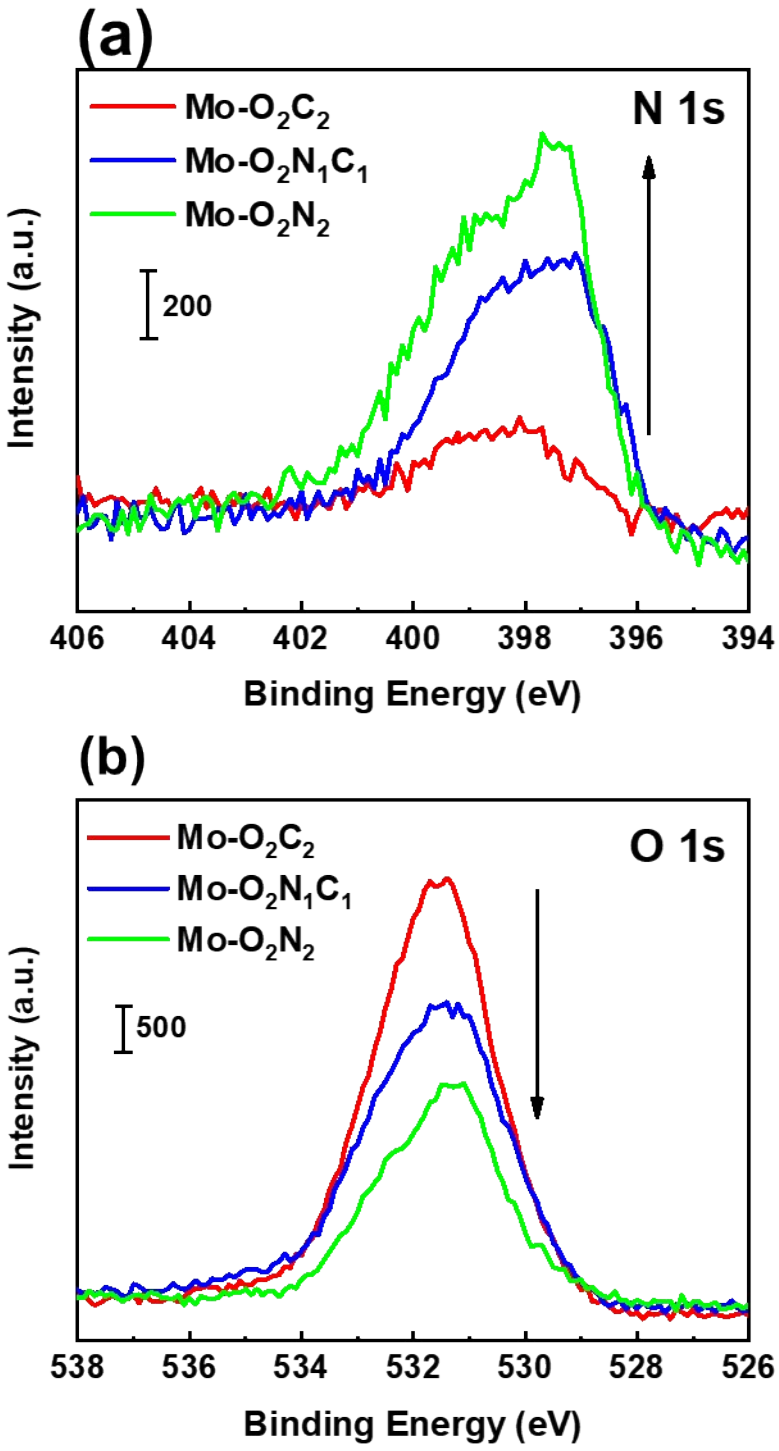

Figure S10. Overlaid HR-XPS spectra of Mo-O_2C_2, Mo-$O_2N_1C_1$, and Mo-O_2N_2. (a) N 1s and (b) O 1s.

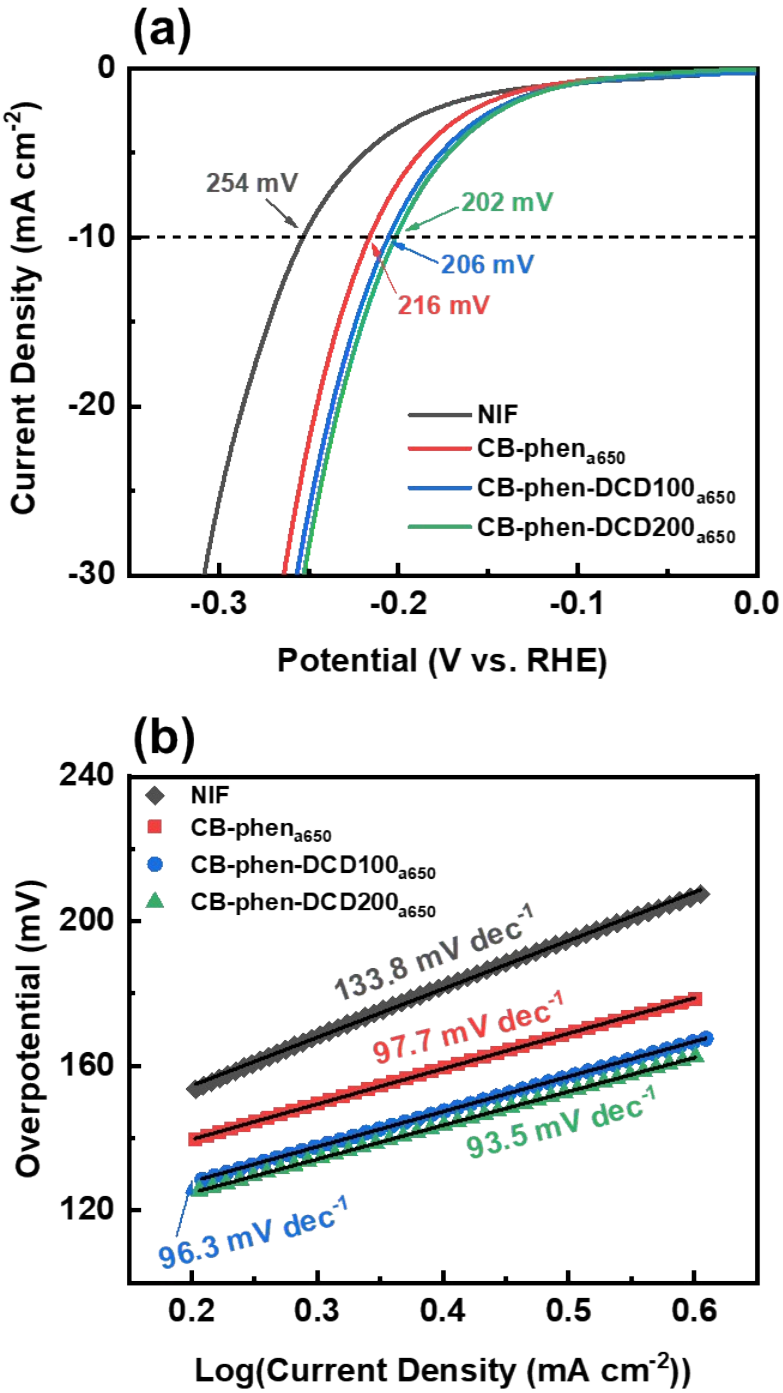

Figure S11. (a) LSV curves and (b) Tafel plots of NIF, CB-phen$_{a650}$, CB-phen-DCD100$_{a650}$, and CB-phen-DCD200$_{a650}$ in 1.0 M KOH. CB-phen$_{a650}$, CB-phen-DCD100$_{a650}$, and CB-phen-DCD200$_{a650}$ are control samples, prepared without presence of Mo precursor, corresponding to Mo-O_2C_2, Mo-$O_2N_1C_1$, and Mo-O_2N_2, respectively.

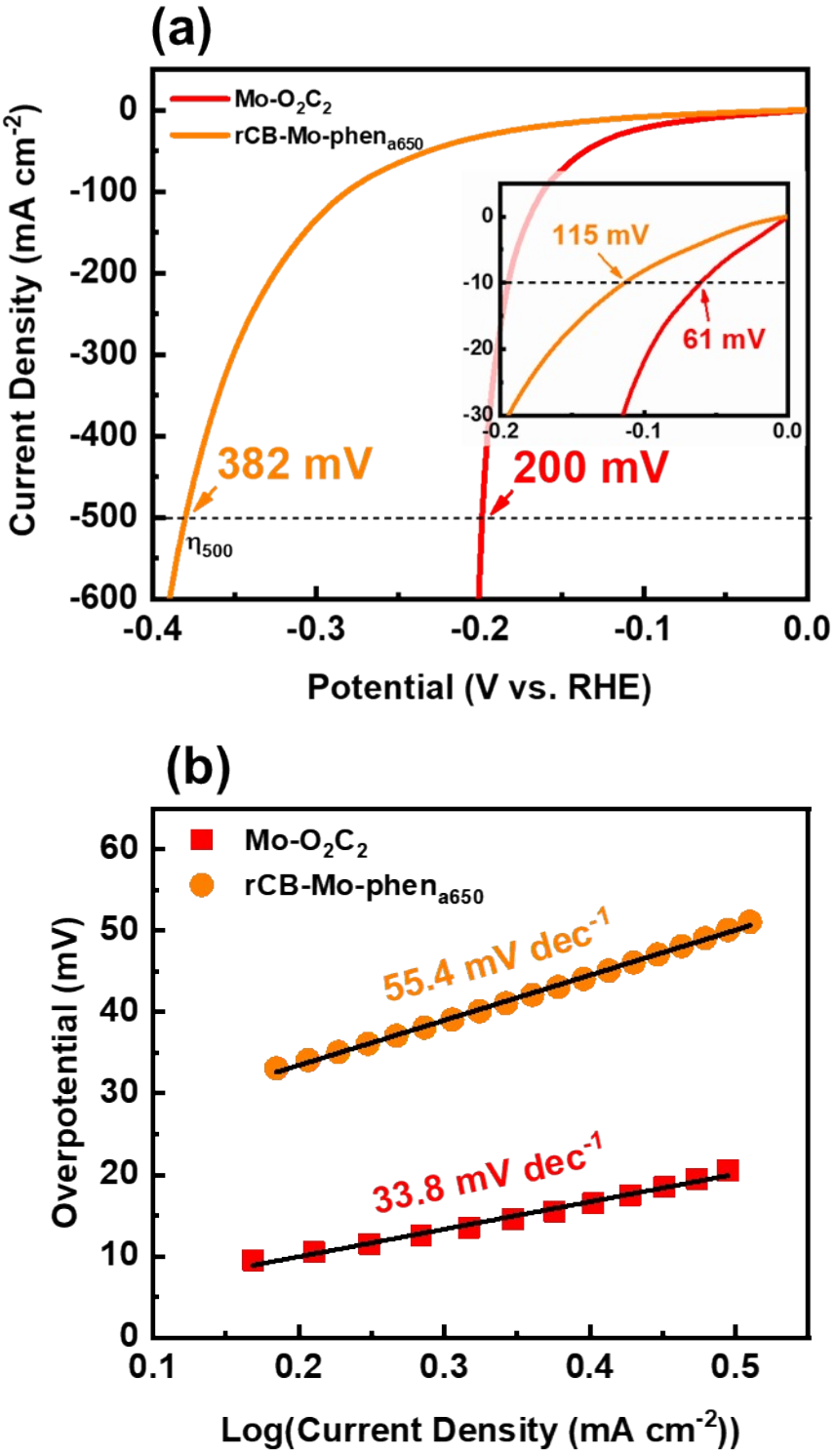

Figure S12. (a) LSV curves and (b) Tafel curves of Mo-O_2C_2 and rCB-Mo-phen$_{a650}$ in 1.0 M KOH.

Table S3. Summary of R_{ct} of sample electrodes determined at -0.17 V (vs. RHE) in 1.0 M KOH.

catalyst	R_{ct} (Ω)
Pt/C	0.70
Mo-O_2C_2	1.32
Mo-$O_2N_1C_1$	2.07
Mo-O_2N_2	2.72

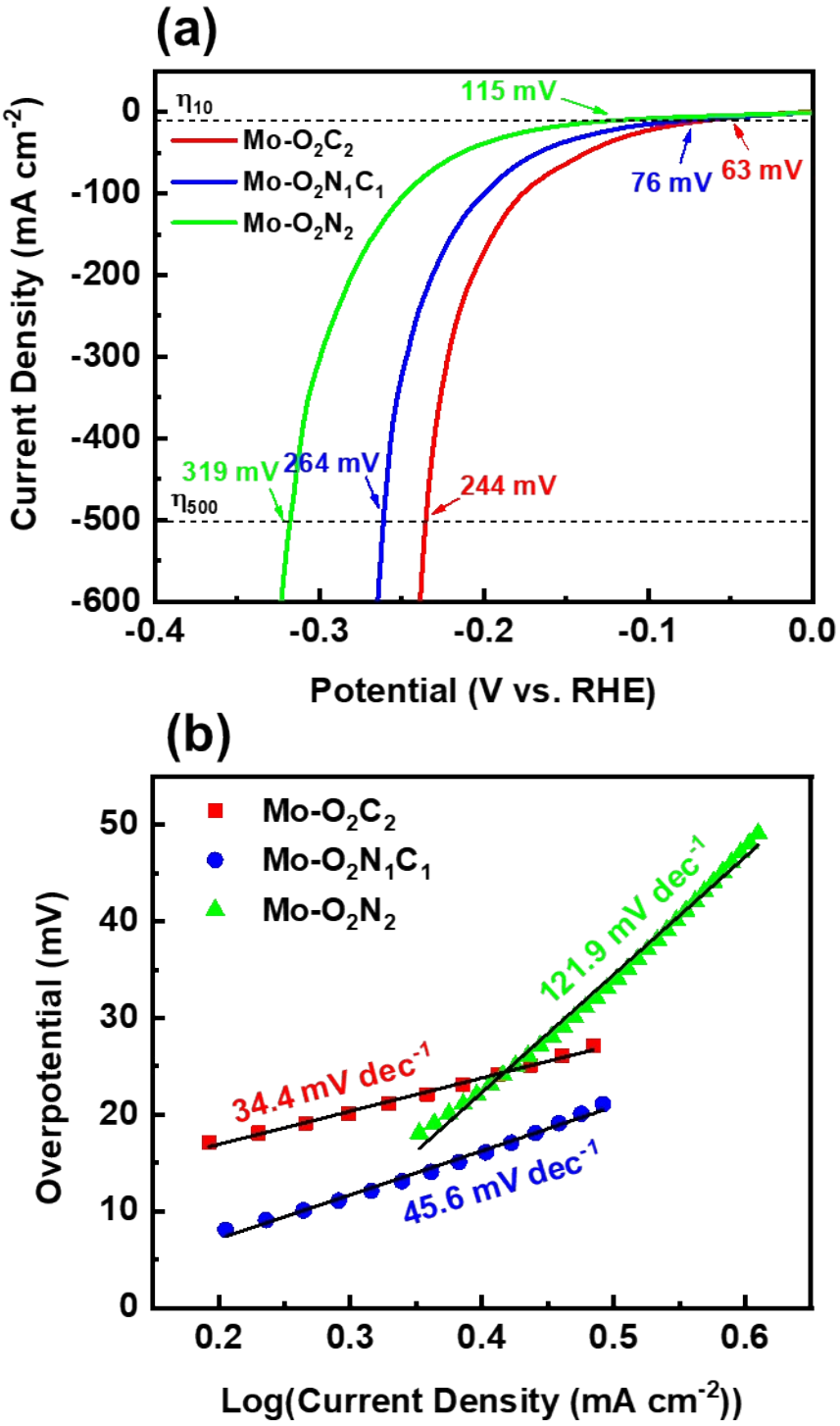

Figure S13. Electrochemical characterizations of Mo-O_2C_2, Mo-$O_2N_1C_1$, and Mo-O_2N_2 in 0.5 M H_2SO_4. (a) LSV curves and (b) Tafel plots.

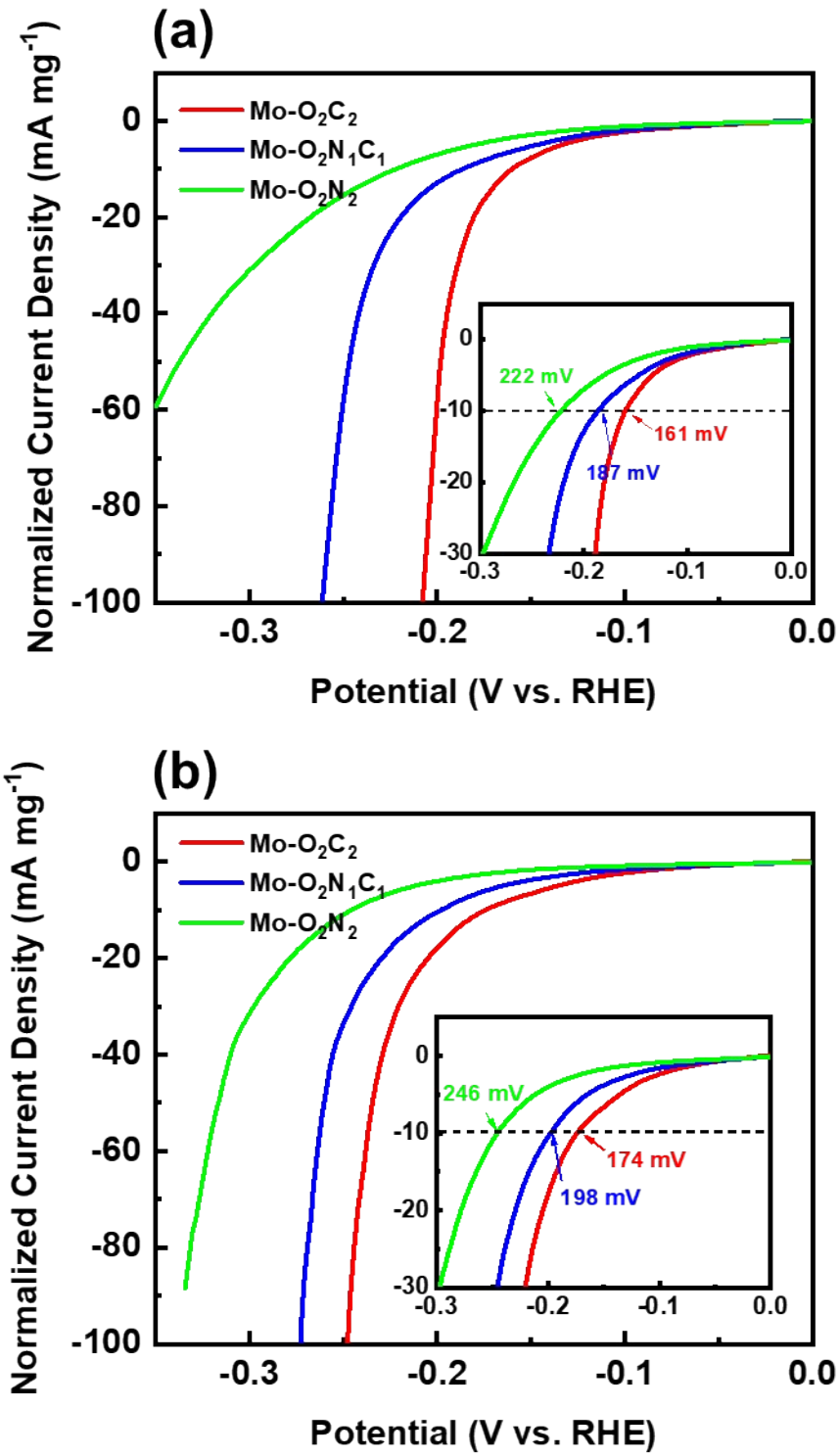

Figure S14. Mass loading normalized LSV curves of Mo-O_2C_2, Mo-$O_2N_1C_1$, and Mo-O_2N_2 in (a) 1.0 M KOH and (b) 0.5 M H_2SO_4. Inset shows LSV curves in low current density region.

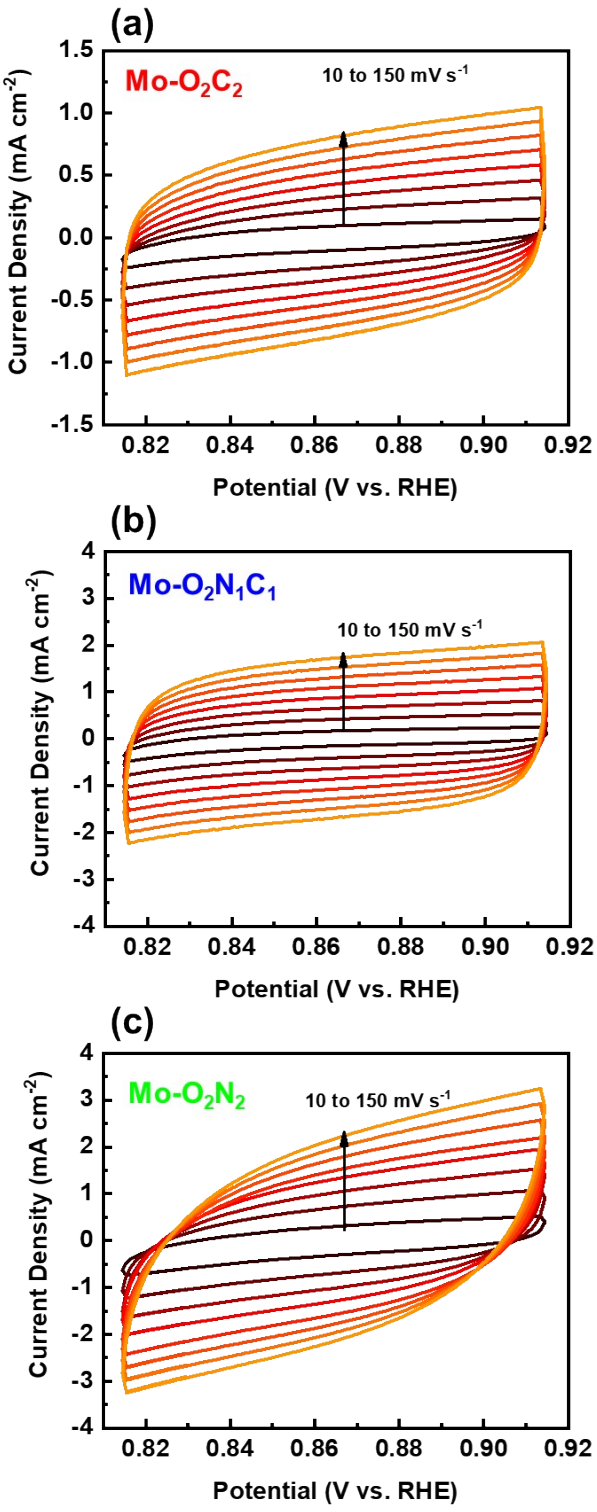

Figure S15. CVs of (a) Mo-O_2C_2, (b) Mo-$O_2N_1C_1$, and (c) Mo-O_2N_2 recorded at increasing scan rates from 10 to 150 mV s^{-1} for estimating of C_{dl} in 1.0 M KOH.

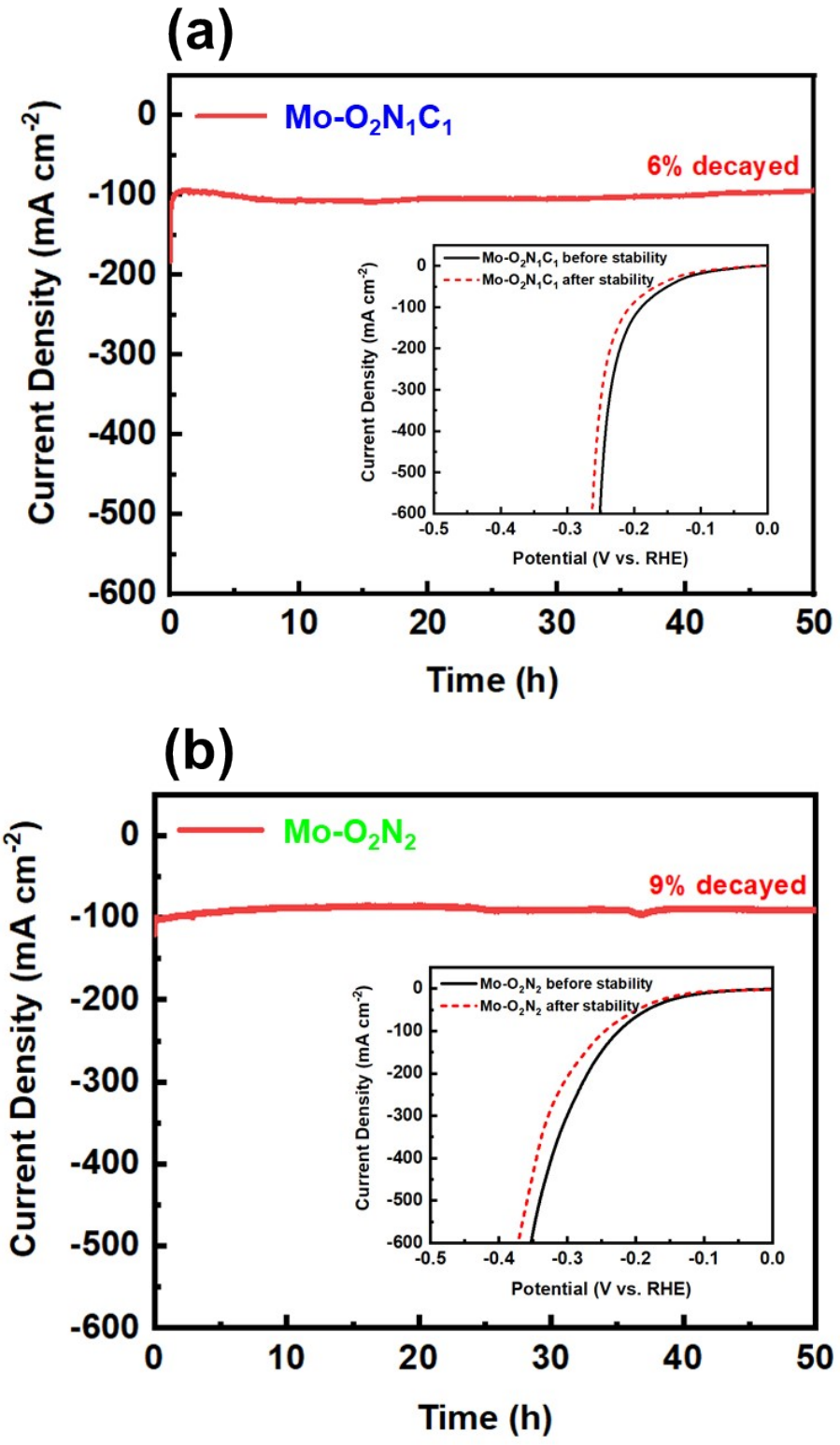

Figure S16. Stability test of (a) Mo-$O_2N_1C_1$ and (b) Mo-O_2N_2 at initial current density of 100 mA cm^{-2} in 1.0 M KOH for 50 h. Inset shows LSV curves before and after stability test.

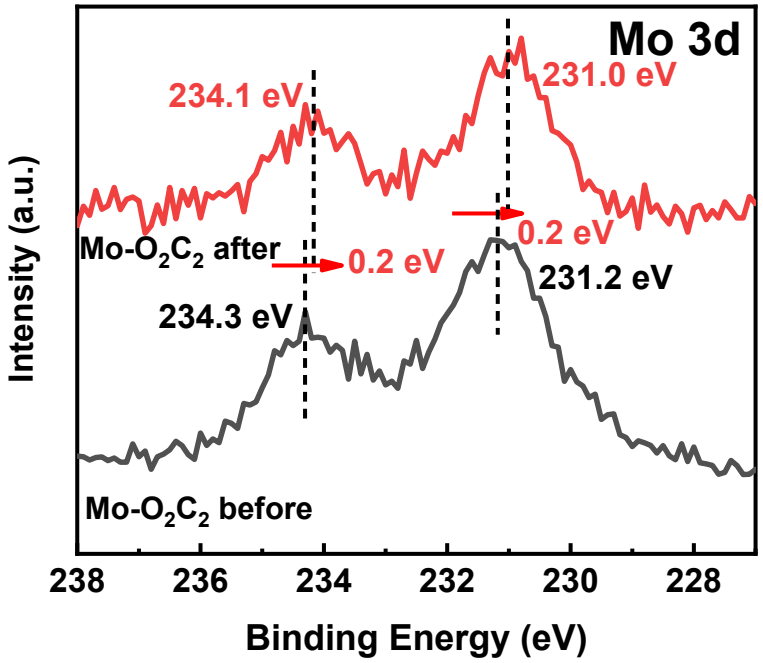

Figure S17. Mo 3d HR-XPS spectra of Mo-O_2C_2 before and after stability test in 1.0 M KOH.

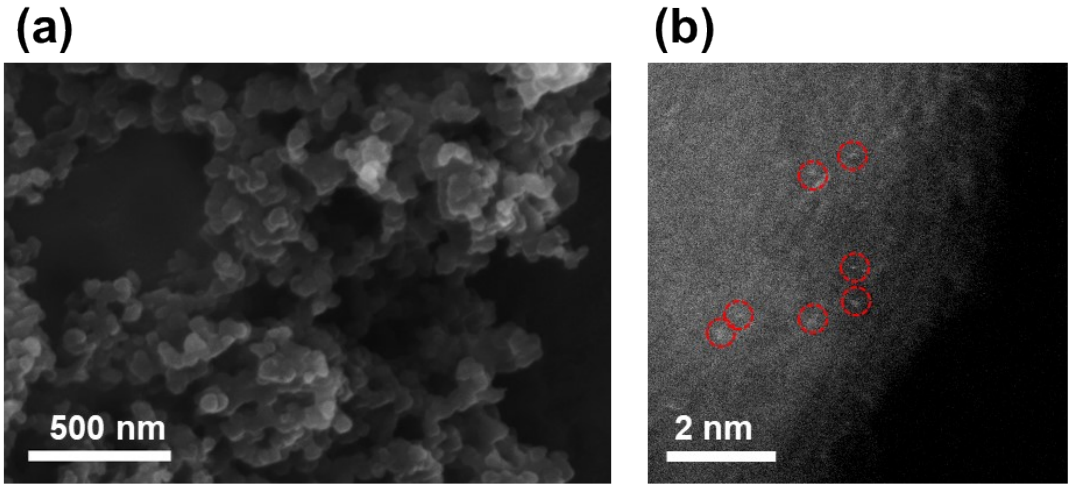

Figure S18. (a) SEM image and (b) high magnification HAADF-STEM image of Mo-O_2C_2 after stability test in 1.0 M KOH. Isolated Mo atoms were marked with red dashed circles.

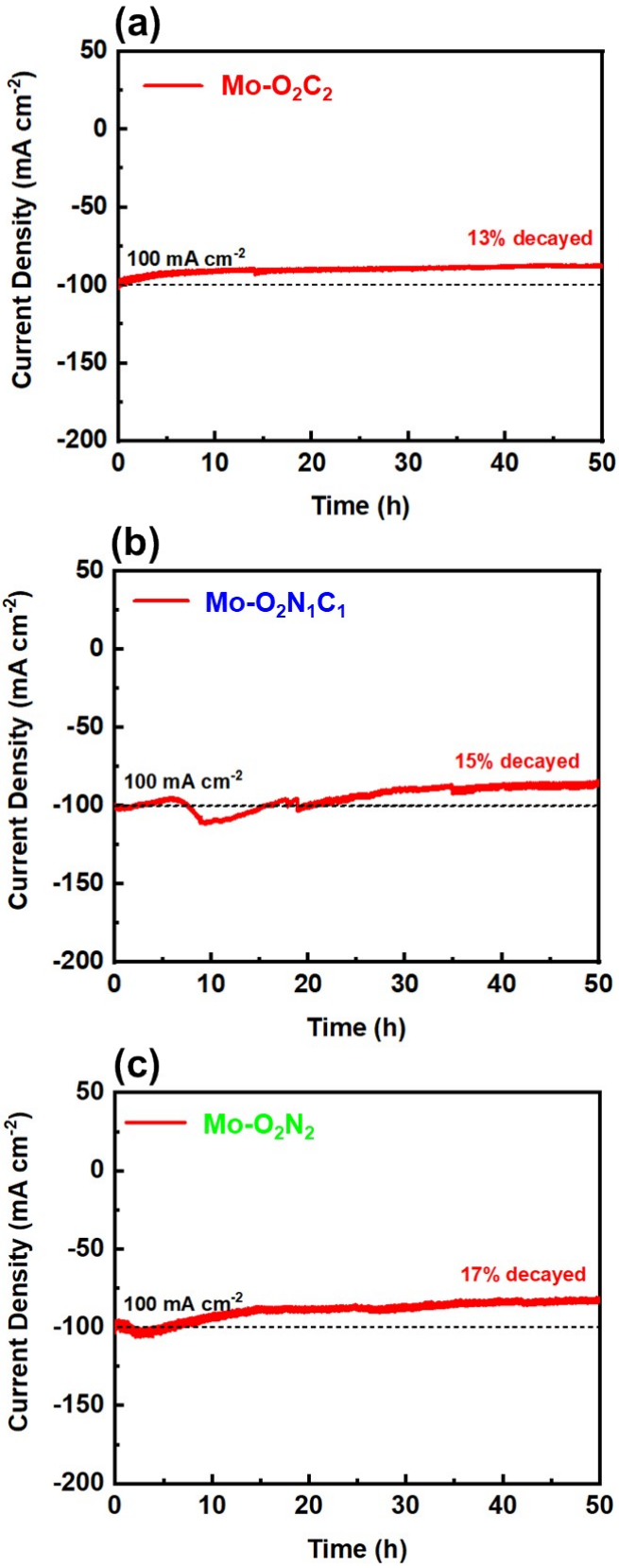

Figure S19. Stability test of (a) Mo-O_2C_2, (b) Mo-$O_2N_1C_1$ and (c) Mo-O_2N_2 at the initial current density of -100 mA cm^{-2} in 0.5 M H_2SO_4 for 50 h.

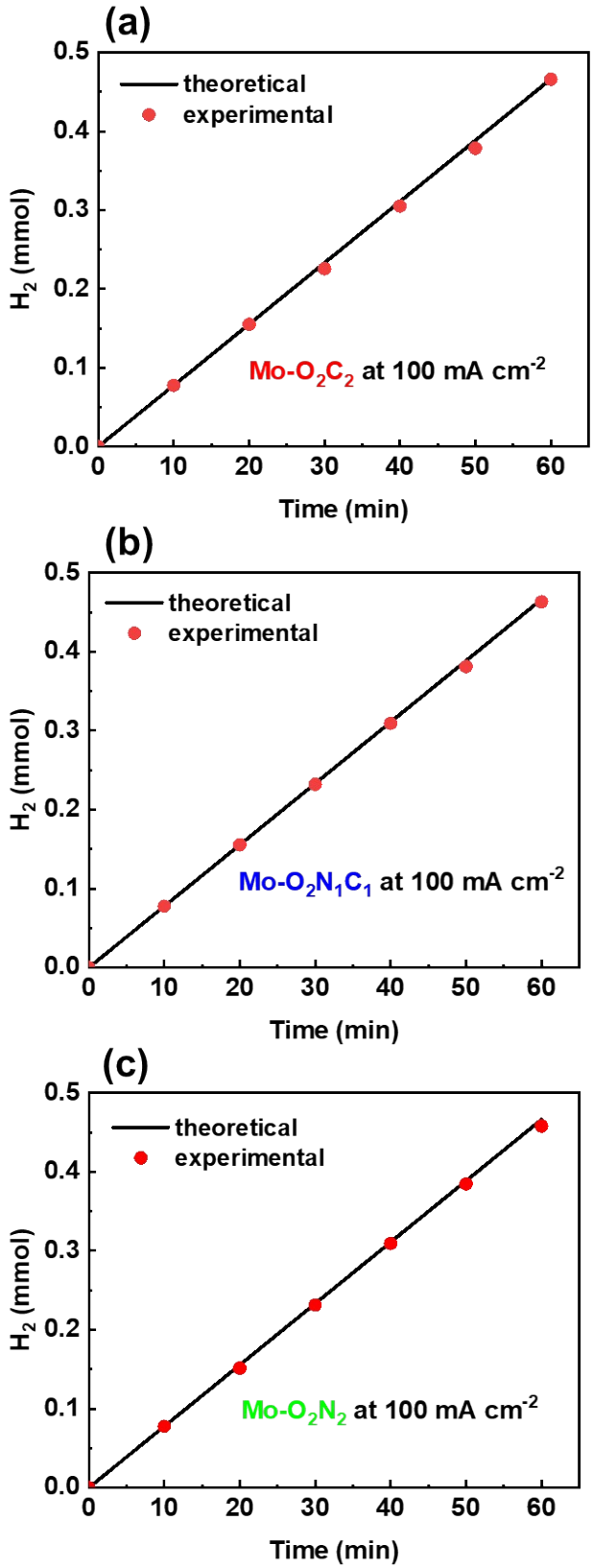

Figure S20. Faradaic efficiency of (a) Mo-O_2C_2, (b) Mo-$O_2N_1C_1$, and (c) Mo-O_2N_2 determined at 100 mA cm^{-2} for 60 minutes in 1.0 M KOH.

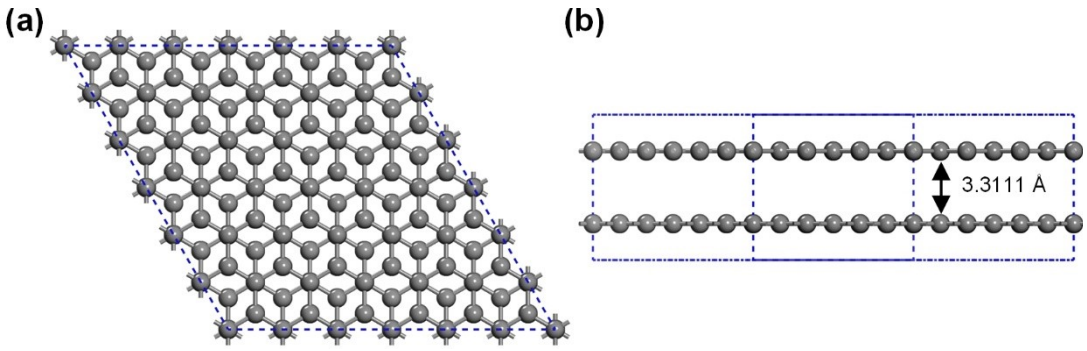

Figure S21. (a) Top and (b) side views of bulk graphite (hexagonal, *P63/mmc*) optimized at RPBE-DFT/D3, resulting in graphite interlayer spacing of 3.3111 Å and CC-bond length of 1.4273 Å. Calculated lattice parameters are a = 2.4722 Å and c = 6.6222 Å.

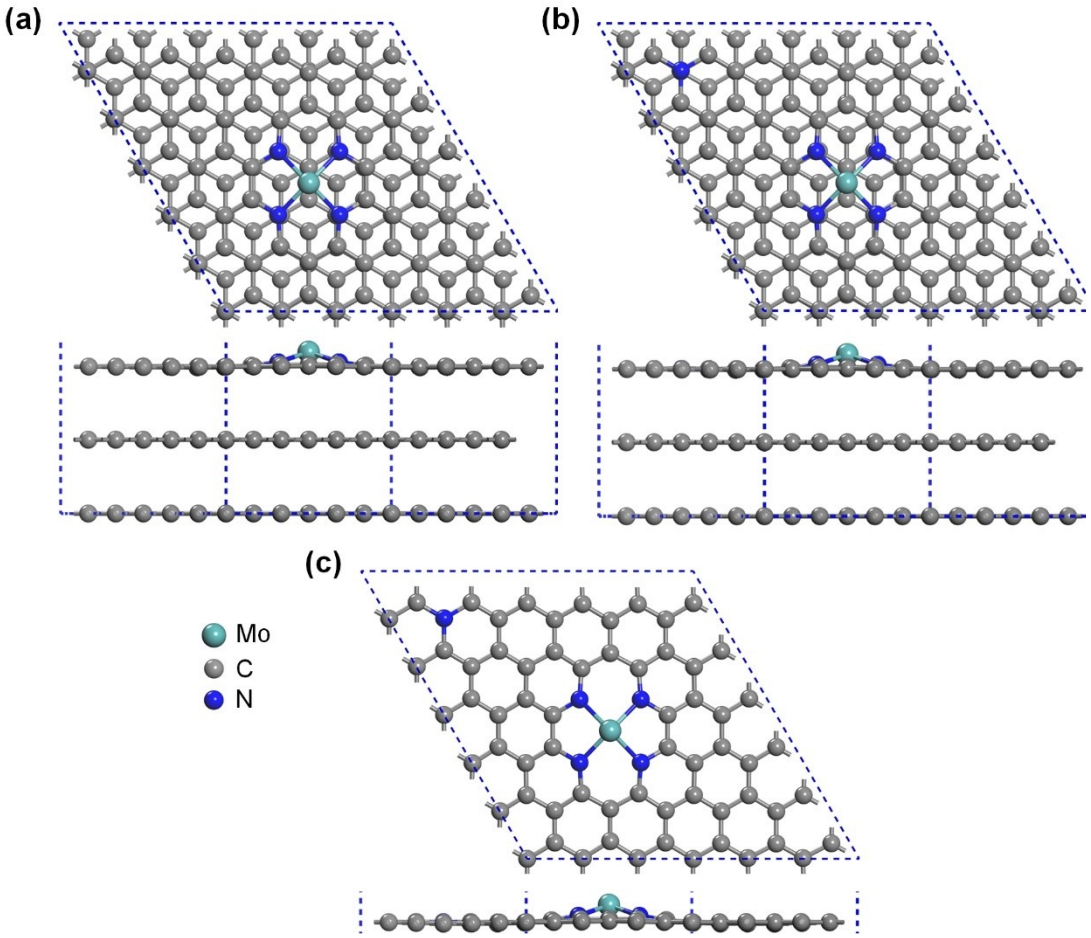

Figure S22. Top and side views of three-layered SA Mo-centered surface models: (a) without and (b) with graphitic N, and (c) one-layer graphene model.

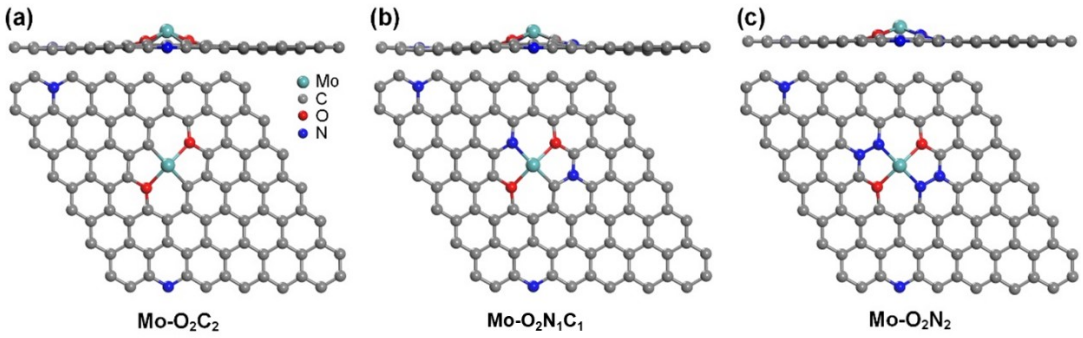

Figure S23. Top and side views of three SA models of (a) Mo-O_2C_2, (b) Mo-$O_2N_1C_1$, and (c) Mo-O_2N_2.

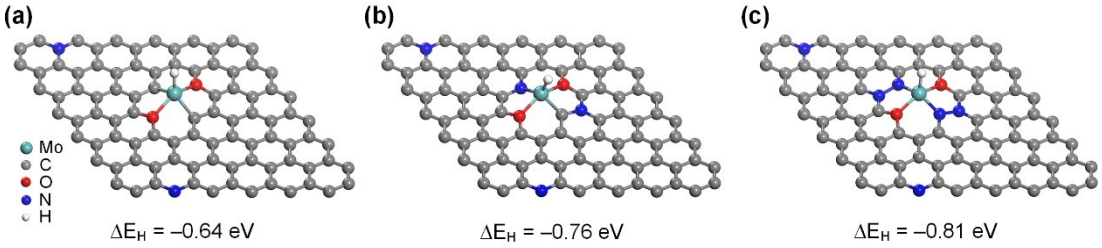

Figure S24. Side views of hydrogen adsorption (ΔE_H) on three SA models of (a) Mo-O_2C_2, (b) Mo-$O_2N_1C_1$, and (c) Mo-O_2N_2.

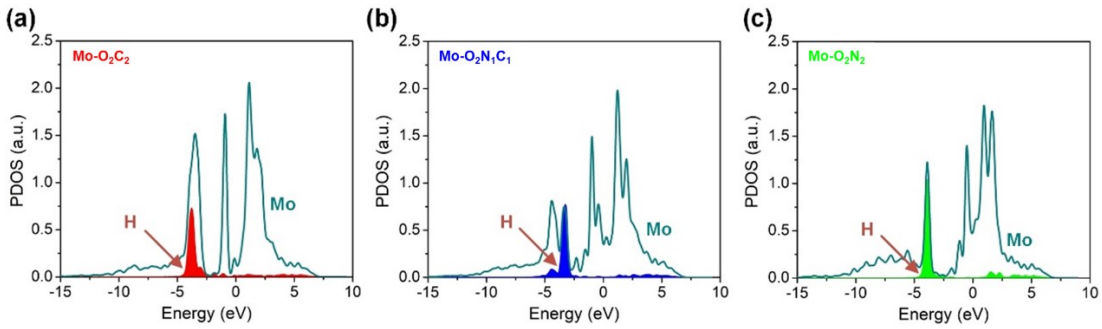

Figure S25. Projected density of states (PDOSs) of orbitals of Mo d and H 1s of hydrogen adsorption on three SA models of (a) Mo-O_2C_2, (b) Mo-$O_2N_1C_1$, and (c) Mo-O_2N_2. Fermi energy level (E_F) is set to zero.

Table S4. (a) Compilation of electronic and thermodynamic properties for H_2. (b) Calculated hydrogen adsorption properties on different surfaces.

(a)	ZPE (eV)	S (kcal/mol K)	S (eV) at 298.15 K	Remark
H_2	0.27	0.032542	0.42	RPBE & RPBE/DFT-D3(BJ)

(b)	ZPE (eV)	ΔE_H (eV)	Correction energy (eV)	ΔG_H (eV)[1]	Remark
Pt(111)	0.175	–0.32	0.25	–0.07 (–0.08)	RPBE
Mo-O_2C_2	0.104	–0.64	0.18	–0.46 (–0.40)	RPBE/DFT-D3(BJ)
Mo-$O_2N_1C_1$	0.107	–0.76	0.18	–0.58 (–0.52)	RPBE/DFT-D3(BJ)
Mo-O_2N_2	0.108	–0.81	0.18	–0.63 (–0.57)	RPBE/DFT-D3(BJ)

[1] Values in parentheses are calculated according to $\Delta G_H = \Delta G_H + 0.24$ and were used to prepare Gibbs energy diagram in the main text.[6]

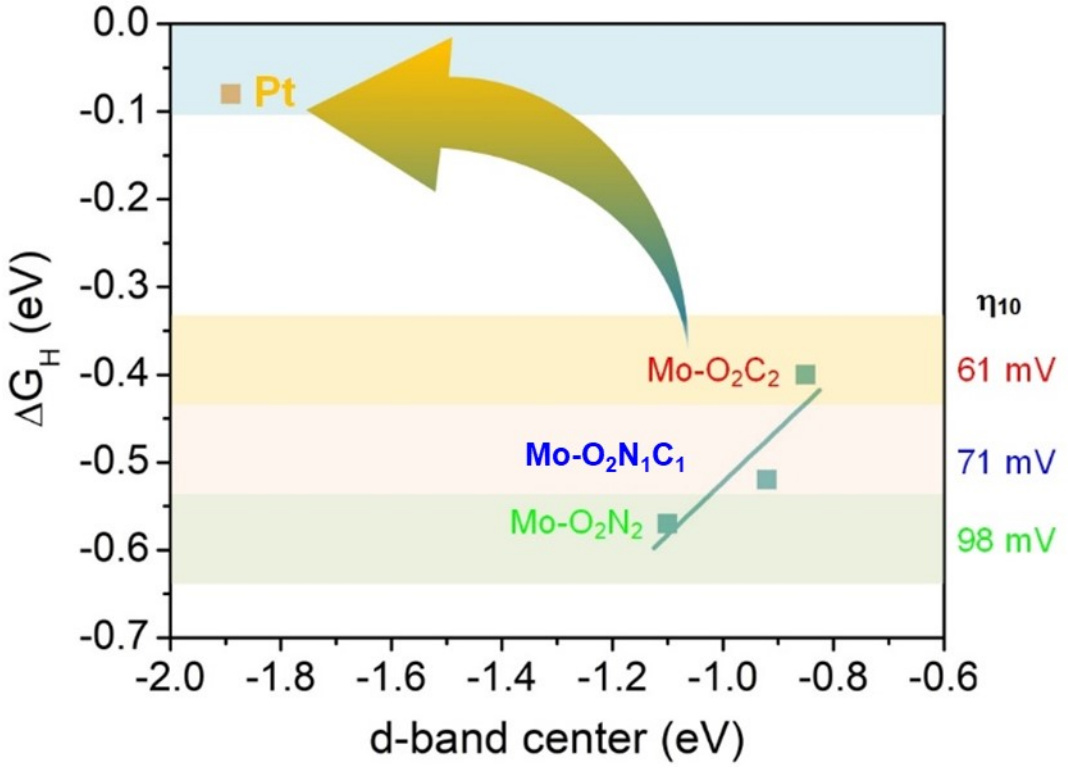

Figure S26. Illustration of calculated Gibbs free energies and overpotentials measured at 10 mA/cm^2 for Mo-O_2C_2, Mo-$O_2N_1C_1$, and Mo-O_2N_2 against d-band center of their Mo metal centers.

Table S5. Comparison of HER efficiency and stability of recently reported state-of-the-art SACs.

Catalyst	SA Concentration	Electrolyte	Over-potential (mV)	Tafel slope (mV dec^{-1})	Stability
Mo-O_2C_2 (this work)	Mo (3.14 wt%)	1.0 M KOH	61(η_{10}), 200(η_{500})	33.8	i-t at -100 mA cm^{-2} for 50 h, 6% decayed
		0.5 M H_2SO_4	63(η_{10}), 244(η_{500})	34.4	i-t at -100 mA cm^{-2} for 50 h, 12% decayed
$Mo_1N_1C_2$[14]	1.32 wt%	0.1 M KOH	132(η_{10})	90	negligible decayed after 1000 CV cycles
Mo-SA@NCA[15]	Mo (18.16 wt%)	1.0 M KOH	~270	N/A	N/A
		0.5 M H_2SO_4	~220	N/A	
Ni/GD[16]	Ni (0.278 wt%)	0.5 M H_2SO	88(η_{10})	45.8	i-t at -10 mA cm^{-2} for 116 h, negligible decayed
Fe/GD[16]	Fe (0.680 wt%)	0.5 M H_2SO_4	66(η_{10})	37.8	i-t at -30 mA cm^{-2} for 60 h, ~20% decayed
Co_1/PCN[17]	Co (0.3 wt%)	1.0 M KOH	138(η_{10})	52	i-t at -10 mA cm^{-2} for 24 h, negligible decayed
Co-D_1T MoS_2[18]	Co (3.54 wt%)	0.5 M H_2SO	42(η_{10})	32	i-t at -34 mA cm^{-2} for 2.8 h,

					negligible decayed
MCM@MoS_2-Ni[19]	Ni (2.7 wt%)	0.5 M H_2SO_4	53(η_{10})	81	i-t at ~62 mA cm^{-2} for 24 h, slightly decayed
W-SAC[20]	W (1.21 wt%)	0.1 M KOH	85(η_{10})	53	i-t at -10 mA cm^{-2} for 11.1 h, ~25% decayed
Pt_1/N-C[21]	Pt (2.5 wt%)	1.0 M KOH	46(η_{10})	36.8	i-t at -10 mA cm^{-2} for 20 h, negligible decayed
		0.5 M H_2SO_4	19(η_{10})	14.2	
Ni_5P_4-Ru[22]	Ru (3.83 wt%)	1.0 M KOH	54(η_{10})	52.0	i-t at -20 mA cm^{-2} for 60 h, than, at -35 mA cm^{-2} for 60 h, negligible decayed
1Pt/VS_2/CP[23]	Pt (3.16 wt%)	0.5 M H_2SO_4	77(η_{10})	40.13	i-t at ~ -18 mA cm^{-2} for 12 h, negligible decayed
Ru SAs/N-Mo_2C NSs[24]	Ru (2.61 wt%)	1.0 M KOH	43(η_{10})	38.67	i-t at ~ -150 mA cm^{-2} for 60 h, slightly decayed
Co-SAC[25]	Co (0.29 at%)	0.5 M H_2SO_4	230(η_{10})	99	slightly decayed after 1000 CV cycles
Ni-SAC[25]	Ni (0.30 at%)		530(η_{10})	167	N/A
W-SAV[25]	W (0.36 at%)		590(η_{10})	122	N/A
CoSAs/PTF-600[26]	Co (0.85 wt%)	0.5 M H_2SO_4	94(η_{10})	50	N/A
CoN_x/C[27]	Co (0.14 wt%)	1.0 M KOH	170(η_{10})	75	N/A
		0.5 M H_2SO_4	133(η_{10})	57	slightly decayed after 5000 CV cycles
$Ni_{sa1.5}$-	Ni (5.01 at%)	1.0 M	196(η_{10})	87	i-t at ~ -10.90

MoS_2[28]		KOH			mA cm^{-2} for 10 h, negligible decayed

References

1. Kresse, G.; Hafner, J., *Phys. Rev. B* **1993,** 47, 558-561.
2. Kresse, G.; Furthmuller, J., *Phys. Rev. B* **1996,** 54, 11169-11186.
3. Perdew, J. P.; Burke, K.; Ernzerhof, M., *Phys. Rev. Lett.* **1996,** 77 (18), 3865-3868.
4. Kresse, G.; Joubert, D., *Phys. Rev. B* **1999,** 59 (3), 1758-1775.
5. Baskin, Y.; Meyer, L., *Phys. Rev.* **1955,** 100 (2), 544-544.
6. Monkhorst, H. J.; Pack, J. D., *Phys. Rev. B* **1976,** 13 (12), 5188-5192.
7. Nørskova, J. K.; Bligaarda, T.; Logadottira, A.; Kitchin, J. R.; Chen, J. G.; Pandelov, S.; Stimming, U., *J. Electrochem. Soc.* **2005,** 152 (3), J23-J26.
8. Furthmüller, J.; Hafner, J.; Kresse, G., *Phys. Rev. B* **1994,** 50 (21), 15606-15622.
9. He Man-Chao, Z. J., *Chin. Phys. B* **2013,** 22 (1), 16802-016802.
10. Delley, B., *J. Chem. Phys.* **1990,** 92 (1), 508-517.
11. Delley, B., *J. Chem. Phys.* **2000,** 113 (18), 7756-7764.
12. Dassault Systèmes BIOVIA. Materials Studio, version 18.1.0.2017, https://www.3dsbiovia.com/ **2018**.
13. Momma, K.; Izum, F., *J. Appl. Crystallogr.* **2011,** 44, 1272-1276.
14. Chen, W.; Pei, J.; He, C. T.; Wan, J.; Ren, H.; Zhu, Y.; Wang, Y.; Dong, J.; Tian, S.; Cheong, W. C., *Angew. Chem. Int. Ed.* **2017,** 56 (50), 16086-16090.
15. Cheng, Y.; Guo, H.; Li, X.; Wu, X.; Xu, X.; Zheng, L.; Song, R., *Chem. Eng. J.* **2021,** 410, 128359.
16. Xue, Y.; Huang, B.; Yi, Y.; Guo, Y.; Zuo, Z.; Li, Y.; Jia, Z.; Liu, H.; Li, Y., *Nature communications* **2018,** 9 (1), 1-10.
17. Cao, L.; Luo, Q.; Liu, W.; Lin, Y.; Liu, X.; Cao, Y.; Zhang, W.; Wu, Y.; Yang, J.; Yao, T., *Nature Catalysis* **2019,** 2 (2), 134-141.
18. Qi, K.; Cui, X.; Gu, L.; Yu, S.; Fan, X.; Luo, M.; Xu, S.; Li, N.; Zheng, L.; Zhang, Q., *Nature communications* **2019,** 10 (1), 1-9.
19. Zhang, H.; Yu, L.; Chen, T.; Zhou, W.; Lou, X. W., *Advanced Functional Materials* **2018,** 28 (51), 1807086.
20. Chen, W.; Pei, J.; He, C. T.; Wan, J.; Ren, H.; Wang, Y.; Dong, J.; Wu, K.; Cheong, W. C.; Mao, J., *Advanced Materials* **2018,** 30 (30), 1800396.
21. Fang, S.; Zhu, X.; Liu, X.; Gu, J.; Liu, W.; Wang, D.; Zhang, W.; Lin, Y.; Lu, J.; Wei, S., *Nature communications* **2020,** 11 (1), 1-8.
22. He, Q.; Tian, D.; Jiang, H.; Cao, D.; Wei, S.; Liu, D.; Song, P.; Lin, Y.; Song, L., *Advanced Materials* **2020,** 32 (11), 1906972.
23. Zhu, J.; Cai, L.; Yin, X.; Wang, Z.; Zhang, L.; Ma, H.; Ke, Y.; Du, Y.; Xi, S.; Wee, A. T., *ACS nano* **2020,** 14 (5), 5600-5608.
24. Yu, J.; Wang, A.; Yu, W.; Liu, X.; Li, X.; Liu, H.; Hu, Y.; Wu, Y.; Zhou, W., *Applied Catalysis B: Environmental* **2020,** 277, 119236.

25. Hossain, M. D.; Liu, Z.; Zhuang, M.; Yan, X.; Xu, G. L.; Gadre, C. A.; Tyagi, A.; Abidi, I. H.; Sun, C. J.; Wong, H., *Advanced Energy Materials* **2019,** 9 (10), 1803689.
26. Yi, J.-D.; Xu, R.; Chai, G.-L.; Zhang, T.; Zang, K.; Nan, B.; Lin, H.; Liang, Y.-L.; Lv, J.; Luo, J., *Journal of Materials Chemistry A* **2019,** 7 (3), 1252-1259.
27. Liang, H.-W.; Brüller, S.; Dong, R.; Zhang, J.; Feng, X.; Müllen, K., *Nature communications* **2015,** 6 (1), 1-8.
28. Zhang, X.; Liu, W.-X.; Zhou, Y.-W.; Meng, Z.-D.; Luo, L.; Liu, S.-Q., *Journal of Electroanalytical Chemistry* **2021,** 894, 115359.